

1510 **Chapter 3**
1511 **Classical Cyclotron**

1512 **Abstract** This chapter introduces the classical cyclotron, and the theoretical material
1513 needed for the simulation exercises. It begins with a brief reminder of the historical
1514 context, and continues with beam optics and with the principles and methods which
1515 the classical cyclotron leans on, including
1516 - ion orbit in a cyclic accelerator,
1517 - weak focusing and periodic transverse motion,
1518 - revolution period and isochronism,
1519 - voltage gap and resonant acceleration,
1520 - the cyclotron equation.

1521 The simulation of a cyclotron dipole will either resort to an analytical model of the
1522 field: the optical element DIPOLE, or will resort to using a field map together with
1523 the keyword TOSCA to handle it and raytrace through. An additional accelerator
1524 device needed in the exercises, CAVITE, simulates a local oscillating voltage. Run-
1525 ning a simulation generates a variety of output files, including the execution listing
1526 zgoubi.res, always, and other zgoubi.plt, zgoubi.CAVITE.out, zgoubi.MATRIX.out,
1527 etc., aimed at looking up program execution, storing data for post-treatment, produc-
1528 ing graphs, etc. Additional keywords are introduced as needed, such as the matching
1529 procedure FIT[2]; FAISCEAU and FAISTORE which log local particle data in
1530 zgoubi.res or in a user defined ancillary file; MARKER; the 'system call' command
1531 SYSTEM; REBELOTE, a 'do loop'; and some more. This chapter introduces in addi-
1532 tion to spin motion in accelerator magnets; dedicated simulation exercises include a
1533 variety of keywords: SPNTRK, a request for spin tracking, SPNPRT or FAISTORE,
1534 to log spin vector components in respectively zgoubi.res or some ancillary file, and
1535 the "IL=2" flag to log stepwise particle data, including spin vector, in zgoubi.plt file.
1536 Simulations include deriving transport matrices, beam matrix, optical functions and
1537 their transport, from rays, using MATRIX and TWISS keywords.

1538 **Notations used in the Text**

$B; B_0$	magnetic field; at a reference radius R_0
$\mathbf{B}; B_R; B_y$	field vector; radial component; axial component
$BR = p/q$	magnetic rigidity
$C; C_0$	orbit length, $C = 2\pi R$; reference, $C_0 = 2\pi R_0$
E	ion energy, $E = \gamma m_0 c^2$
$f_{\text{rev}}, f_{\text{rf}}$	revolution and RF voltage frequencies
G	gyromagnetic anomaly, $G = 1.7928$ for proton, -4.184 for helion
h	harmonic number, an integer, $h = f_{\text{rf}}/f_{\text{rev}}$
$k = \frac{R}{B} \frac{dB}{dR}$	radial field index
$m; m_0; M$	ion mass; rest mass; in units of MeV/c^2
$\mathbf{p}; p; p_0$	ion momentum vector; its modulus; reference
q	ion charge
$R; R_0; R_E$	equilibrium orbit radius; reference, $R(p_0)$; at energy E
RF	Radio-Frequency
1539 s	path variable
$T_{\text{rev}}, T_{\text{rf}}$	revolution and accelerating voltage periods
$\mathbf{v}; v$	ion velocity vector; its modulus
$V(t); \hat{V}$	oscillating voltage; its peak value
W	kinetic energy, $W = \frac{1}{2}mv^2$
x, x', y, y'	radial and axial coordinates $\left[(*)' = \frac{d(*)}{ds} \right]$
α	trajectory deviation, or momentum compaction
$\beta = \frac{v}{c}; \beta_0; \beta_s$	normalized ion velocity; reference; synchronous
$\gamma = E/m_0c^2$	Lorentz relativistic factor
$\Delta p, \delta p$	momentum offset
ε_u	Courant-Snyder invariant ($u : x, r, y, l, Y, Z, s, \text{etc.}$)
θ	azimuthal angle
ϕ	RF phase at ion arrival at the voltage gap

1540 **3.1 Introduction**

1541 Cyclotrons are the most widespread type of accelerator, today, used by thousands,
 1542 with the production of isotopes as the dominant application. This chapter is devoted
 1543 to the first cyclic accelerator: the early 1930s *classical* cyclotron which its concept
 1544 limited to low energy, a few 10s of $\text{MeV}/\text{nucleon}$. This limitation overcome a decade
 1545 later by the azimuthally varying field (AVF) technique, this is the subject of the next
 1546 chapter.

1547 The classical cyclotron is based on four main principles:

1548 (i) the use of a cylindrical-symmetry magnetic field in the gap of an electromagnet
 1549 (Fig. 3.1) to maintain ions on a circular trajectory

- 1550 (ii) transverse vertical confinement of the beam obtained by a slow radial decrease
 1551 of the magnetic field. A technique known as weak focusing, applied over the years
 1552 in all cyclic accelerators: microtron, betatron, synchrocyclotron, synchrotron. These
 1553 weak focusing accelerator species all are still part of the landscape today
 1554 (iii) resonant acceleration by synchronization of a fixed-frequency accelerating volt-
 1555 age on the quasi-constant revolution time (Fig. 3.1). and
 1556 (iv) use of high voltage, to mitigate the effect of the turn-by-turn RF phase slip.

1557 Resonant acceleration has the advantage that a small gap voltage is enough to
 1558 accelerate with, in principle, no energy limitation, by contrast with the electrostatic
 1559 techniques developed at the time, which required the generation of the full voltage,
 1560 such as the Van de Graaf which was limited by sparking at a few tens of megavolts.

1561 The cyclotron concept goes back to the late 1920s [1], yet it was not until the early
 1562 1930s when a cyclotron was first brought to operation [2]. The principles are sum-
 1563 marized in Fig. 3.1: an oscillating voltage is applied on a pair of electrodes (“dees”)
 1564 forming an accelerating gap and placed between the two poles of an electromagnet.
 1565 Ions reaching the gap during the acceleration phase of the voltage wave experience
 1566 an energy boost; no field is experienced inside the dees. Under the effect of energy
 1567 increase at the gap every half-revolution, they spiral out in the quasi-constant field
 of the dipole.

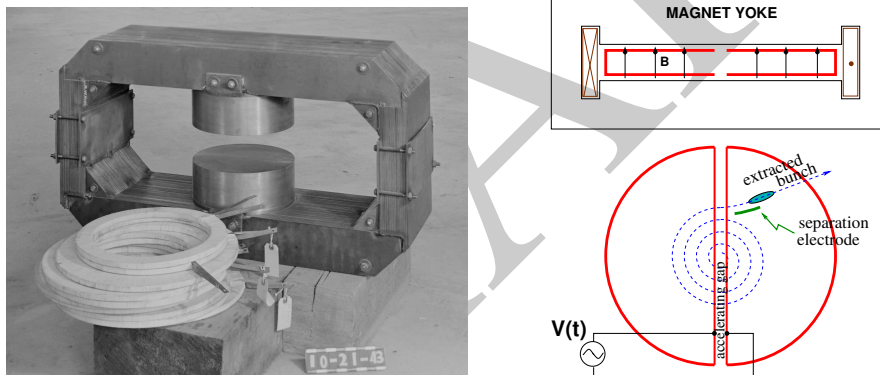


Fig. 3.1 Left: a cyclotron electromagnet, namely here that used for a model of Berkeley’s 184-inch cyclotron in the early 1940s [3]. Magnetic field in the gap decreases with radius. Right: a schematic of the resonant acceleration motion; gap after gap, accelerated ions spiral out (bottom) in the quasi-uniform field (top). A double-dee (or, a variant, a single-dee facing a slotted electrode) forms an accelerating gap. The fixed-frequency oscillating voltage $V(t)$ applied is a harmonic of the revolution frequency. Ions experiencing proper voltage phase at the gap, turn by turn, are accelerated. A septum electrode allows beam extraction

1568 The first cyclotron achieved acceleration of H_2^+ hydrogen ions to 80 keV [2], at
 1569 Berkeley in 1931. The apparatus used a dee-shaped electrode vis-à-vis a slotted
 1570 electrode forming a voltage gap, the ensemble housed in a 5 in diameter vacuum
 1571 chamber and placed in the 1.3 Tesla field of an electromagnet. A ≈ 12 MHz vacuum
 1572 tube oscillator provided 1 kVolt gap voltage.
 1573

1574 One goal foreseen in developing this technology was the acceleration of protons
 1575 to MeV energy range for the study of atom nucleus. And in background, a wealth
 1576 of potential applications. An 11 in cyclotron followed which delivered a $0.01 \mu\text{A}$
 1577 H_2^+ beam at 1.22 MeV [4], and a 27 in cyclotron later reached 6 MeV (Fig. 3.2) [5].
 1578 Targets were mounted at the periphery of the 11-inch cyclotron, disintegrations were
 1579 observed in 1932. And, in 1933: *'The neutron had been identified by Chadwick*
 1580 *in 1932. By 1933 we were producing and observing neutrons from every target*
 1581 *bombarded by deuterons.'* [5, M.S. Livingston, p. 22].

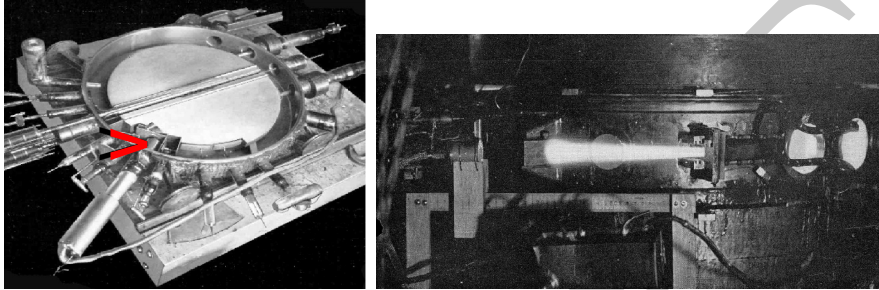
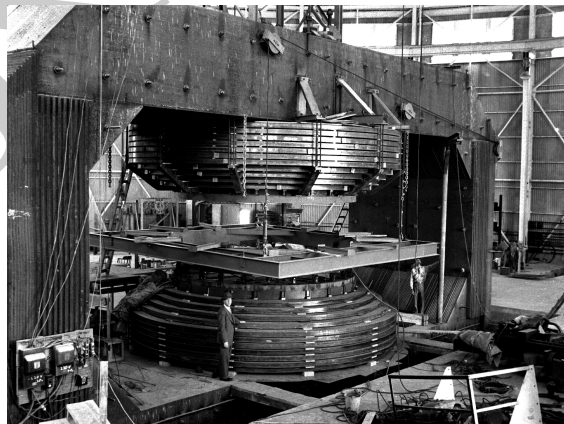


Fig. 3.2 Berkeley 27-inch cyclotron, brought to operation in 1934, accelerated deuterons up to 6 MeV. Left: a double-dee (seen in the vacuum chamber, cover off), 22 in diameter, creates an accelerating gap: 13 kV, 12 MHz radio frequency voltage is applied for deuterons for instance (through two feed lines seen at the top right corner). This apparatus was dipped in the 1.6 Tesla dipole field of a 27 in diameter, 75 ton, electromagnet. A slight decrease of the dipole field with radius, from the center of the dipole, ensures axial beam focusing. With their energy increasing, ions spiral out from the center to eventually strike a target (red arrow). Right: ionization of the air by the extracted beam (1936); the view also shows the vacuum chamber squeezed between the pole pieces of the electromagnet [3]

Fig. 3.3 Berkeley 184 in diameter, 4,000 ton cyclotron during construction [3]. The coil windings around both of the magnetic poles are clearly visible. Following the invention of longitudinal focusing it was actually operated as a synchrocyclotron, in 1946. The man on the right gives the scale



1582 A broad range of applications were foreseen: “*At this time biological experiments*
1583 *were started. [...] Also at about this same time the first radioactive tracer experiments*
1584 *on human beings were tried [...] simple beginnings of therapeutic use, coming a*
1585 *little bit later, in which neutron radiation was used, for instance, in the treatment*
1586 *of cancer. [...] Another highlight from 1936 was the first time that anyone tried*
1587 *to make artificially a naturally occurring radio-nuclide. (a bismuth isotope) [5,*
1588 *McMillan, p. 26].*

1589 Berkeley’s 184 in cyclotron, the largest (Fig. 3.3), commissioned in 1941, was to
1590 accelerate Deuterons to 100 MeV for meson production. It’s magnet however was
1591 diverted to the production of uranium for the atomic bomb during the second world
1592 war years [1]. Re-started in 1946, as a consequence of the discovery of phase focusing
1593 the accelerator was actually operated as a synchrocyclotron (an accelerator species
1594 addressed in Chap. 7).

1595 *Limitation in energy*

1596 The understanding of the dynamics of ions in the classical cyclotron took some time,
1597 and brought two news, a bad one and a good one,

1598 (i) the bad one first: the energy limitation. A consequence of the loss of isochro-
1599 nism resulting from the relativistic increase of the ion mass so that “[...] *it seems*
1600 *useless to build cyclotrons of larger proportions than the existing ones [...] an accel-*
1601 *erating chamber of 37 in radius will suffice to produce deuterons of 11 MeV energy*
1602 *which is the highest possible [...] [6], or in a different form: “If you went to graduate*
1603 *school in the 1940s, this inequality ($-1 < k < 0$) was the end of the discussion of*
1604 *accelerator theory” [7].*

1605 (ii) the good news now: the energy limit which results from the mass increase can
1606 be removed by splitting the magnetic pole into valley and hill field sectors. This is
1607 the azimuthally varying field (AVF) cyclotron technology, due to L.H. Thomas in
1608 1938 [8]. It took some years to see effects of this breakthrough (Fig. 3.4). The AVF
1609 is the object of Chap. 4.

1610 With the progress in magnet computation tools, in computer speed and in beam
1611 dynamics simulations, the AVF cyclotron ends up being essentially as simple to
1612 design and build: it has in a general manner supplanted the classical cyclotron in all
1613 energy domains (Fig. 3.4).

1614 **3.2 Basic Concepts and Formulæ**

1615 The cyclotron was conceived as a means to overcome the technological difficulty of
1616 a long series of high electrostatic voltage electrodes in a linear layout, by, instead,
1617 repeated recirculation through a single accelerating gap in synchronism with an
1618 oscillating voltage (Fig. 3.5). As the accelerated bunch spirals out in the uniform
1619 magnetic field, the velocity increase comes with an increase in orbit length; the

Fig. 3.4 Evolution of the number of the various cyclotron species, over the years [9]. From the 1950s on the AVF cyclotron rapidly supplanted the 1930s' classical cyclotron

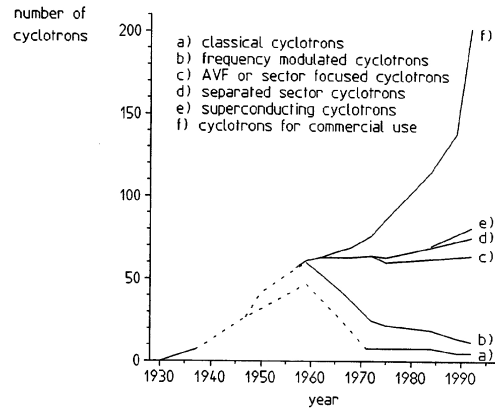


Fig. 3.5 Resonant acceleration: in an $h = 1$ configuration an ion bunch meets an oscillating field \mathbf{E} across gap A, at time t , at an accelerating phase; it meets again, half a turn later, at time $t + T_{rev}/2$, the accelerating phase across gap A', and so on: the magnetic field recirculates the bunch through the gap, repeatedly. Higher harmonic allows more bunches: the next possibility in the present configuration is $h=3$, and 3 bunches, 120 degrees apart, in synchronism with \mathbf{E}

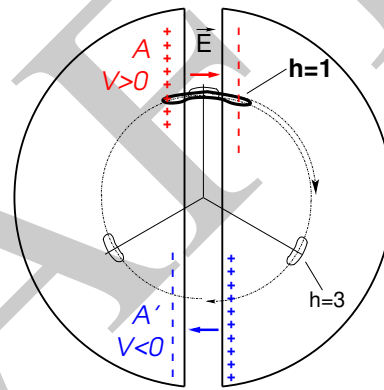
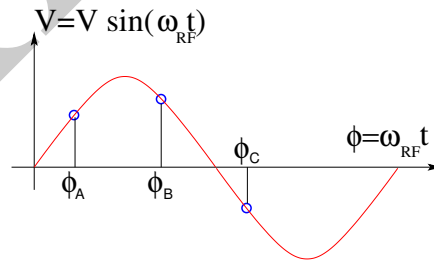


Fig. 3.6 An ion which reaches the double-dee gap at the RF phase $\omega_{rf}t = \phi_A$ or $\omega_{rf}t = \phi_B$ is accelerated. If it reaches the gap at $\omega_{rf}t = \phi_C$ it is decelerated



1620 net result is a slow increase of the revolution period T_{rev} with energy, yet, with
 1621 appropriate fixed $f_{\text{rf}} \approx h/T_{\text{rev}}$ the revolution motion and the oscillating voltage can
 1622 be maintained in sufficiently close synchronism, $T_{\text{rev}} \approx T_{\text{rf}}/h$, that the bunch will
 1623 transit the voltage gap at an accelerating phase (Fig. 3.6) over a large enough number
 1624 of turns that it acquires a significant energy boost.

1625 The orbital motion quantities: radius R , ion rigidity BR , revolution frequency
 1626 f_{rev} , satisfy

$$BR = \frac{p}{q}, \quad 2\pi f_{\text{rev}} = \omega_{\text{rev}} = \frac{v}{R} = \frac{qB}{m} = \frac{qB}{\gamma m_0} \quad (3.1)$$

1627 These relationships hold at all γ , so covering the *classical* cyclotron domain ($v \ll c$,
 1628 $\gamma \approx 1$) as well as the *isochronous* cyclotron (in which the ion energy increase is
 1629 commensurate with its mass). To give an idea of the revolution frequency, in the
 1630 limit $\gamma = 1$, for protons, one has $f_{\text{rev}}/B = q/2\pi m = 15.25 \text{ MHz/T}$.

1631 The cyclotron design sets the constant RF frequency $f_{\text{rf}} = \omega_{\text{rf}}/2\pi$ at an interme-
 1632 diate value of hf_{rev} along the acceleration cycle. The energy gain, or loss, by the ion
 1633 when transiting the gap, at time t , is

$$\Delta W(t) = q\hat{V} \sin \phi(t) \quad \text{with} \quad \phi(t) = \omega_{\text{rf}}t - \omega_{\text{rev}}t + \phi_0 \quad (3.2)$$

1634 with ϕ its phase with respect to the RF signal at the gap (Fig. 3.6), $\phi_0 = \phi(t=0)$,
 1635 and $\omega_{\text{rev}}t$ the orbital angle. Assuming constant field B , the increase of the revolution
 1636 period with ion energy satisfies

$$\frac{\Delta T_{\text{rev}}}{T_{\text{rev}}} = \gamma - 1 \quad (3.3)$$

1637 The mis-match so induced between the RF and cyclotron frequencies is a turn-by-turn
 1638 cumulative effect and sets a limit to the tolerable isochronism defect, $\Delta T_{\text{rev}}/T_{\text{rev}} \approx$
 1639 $2 - 3\%$, or highest velocity $\beta = v/c \approx 0.22$. This results for instance in a practical
 1640 limitation to $\approx 25 \text{ MeV}$ for protons, and $\approx 50 \text{ MeV}$ for D and α particles, a limit
 1641 however dependent on energy gain per turn.

1642 Over time multiple-gap accelerating structures were developed, whereby a
 1643 “multiple- Δ ” electrode pattern substitutes to a “double-D”. An example is GANIL
 1644 C0 injector with its 4 accelerating gaps and $h = 4$ and $h = 8$ RF harmonic opera-
 1645 tion [10].

1646 3.2.1 Fixed-Energy Orbits, Revolution Period

In a laboratory frame (O;x,y,z), with (O;x,z) the bend plane (Fig. 3.7), assume
 $\mathbf{B}|_{y=0} = \mathbf{B}_y$, constant. An ion is launched from the origin with a velocity

$$\mathbf{v} = \left(\frac{dx}{dt}, \frac{dy}{dt}, \frac{dz}{dt} \right) = (v \sin \alpha, 0, v \cos \alpha)$$

at an angle α from the z -axis. Solving

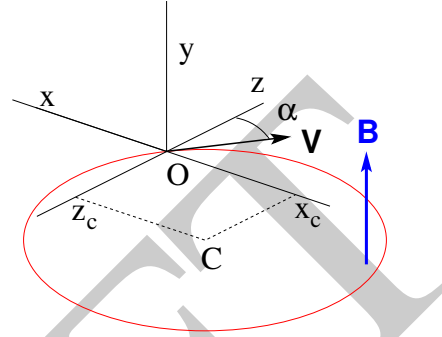


Fig. 3.7 Circular motion of an ion in the plane normal to a uniform magnetic field \mathbf{B} . The orbit is centered at $x_C = -v \cos \alpha / \omega_{\text{rev}}$, $z_C = v \sin \alpha / \omega_{\text{rev}}$, its radius is v / ω_{rev}

1647

$$m\dot{\mathbf{v}} = q\mathbf{v} \times \mathbf{B} \quad (3.4)$$

1648 with $\mathbf{B} = (0, B_y, 0)$ yields the parametric equations of motion

$$\begin{cases} x(t) = \frac{v}{\omega_{\text{rev}}} \cos(\omega_{\text{rev}}t - \alpha) - \frac{v \cos \alpha}{\omega_{\text{rev}}} \\ y(t) = \text{constant} \\ z(t) = \frac{v}{\omega_{\text{rev}}} \sin(\omega_{\text{rev}}t - \alpha) + \frac{v \sin \alpha}{\omega_{\text{rev}}} \end{cases} \quad (3.5)$$

1649 which result in

$$\left(x + \frac{v \cos \alpha}{\omega_{\text{rev}}}\right)^2 + \left(z - \frac{v \sin \alpha}{\omega_{\text{rev}}}\right)^2 = \left(\frac{v}{\omega_{\text{rev}}}\right)^2 \quad (3.6)$$

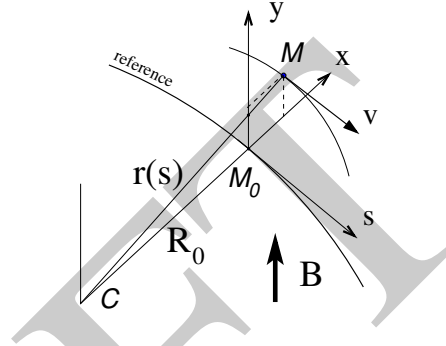
1650 a circular trajectory of radius $R = v / \omega_{\text{rev}}$ centered at $(x_C, z_C) = \left(-\frac{v \cos \alpha}{\omega_{\text{rev}}}, \frac{v \sin \alpha}{\omega_{\text{rev}}}\right)$.

1651 *Stability of the cyclic motion* - The initial velocity vector defines a reference closed
 1652 orbit in the median plane of the cyclotron dipole; a small perturbation in α or v
 1653 results in a new orbit *in the vicinity* of the reference. An axial velocity component v_y
 1654 on the other hand, causes the ion to drift away from the reference, vertically, linearly
 1655 with time, as there is no axial restoring force. The next Section will investigate the
 1656 necessary field property to ensure both horizontal and vertical confinement of the
 1657 cyclic motion in the vicinity of a reference orbit in the median plane.

1658 3.2.2 Weak Focusing

1659 In the early accelerated turns in a classical cyclotron (central region of the electro-
 1660 magnet, energy up to tens of keV/u), the accelerating electric field provides vertical
 1661 focusing for particles with proper RF phase [11, Sect. 8], whereas a flat magnetic
 1662 field with uniformity $dB/B < 10^{-4}$ is sufficient to maintain isochronism. Beyond
 1663 this low energy region however, at greater radii, a magnetic field gradient must be
 1664 introduced to ensure transverse stability: field must decrease with R .

Fig. 3.8 Moving frame $(M_0; s, x, y)$ along the reference circular orbit. The curvature $1/R_0$ is constant along the orbit and $(M_0; s, x, y)$ can be considered equivalent to the cylindrical frame $(C; \theta, R_0, y)$



1665 Ion coordinates in the following are defined in the moving frame $(M_0; s, x, y)$
 1666 (Fig. 3.8), which moves along the reference orbit (radius R_0), with its origin M_0
 1667 the projection of ion location M on the reference orbit; the s axis is tangent to the
 1668 latter, the x axis is normal to s , the y axis is normal to the bend plane. Median-plane
 1669 symmetry of the field is assumed, thus the radial field component $B_R|_{y=0} = 0$ at all
 1670 R (Fig. 3.9).

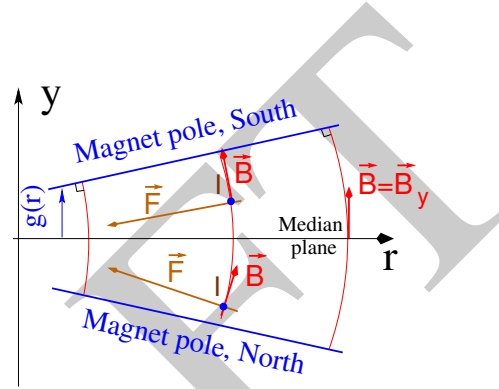
1671 Consider small motion excursions $x(t) = r(t) - R_0 \ll R_0$; introduce Taylor
 1672 expansion of the field components,

$$\begin{aligned}
 B_y(R_0 + x) &= B_y(R_0) + x \left. \frac{\partial B_y}{\partial R} \right|_{R_0} + \frac{x^2}{2!} \left. \frac{\partial^2 B_y}{\partial R^2} \right|_{R_0} + \dots \approx B_y(R_0) + x \left. \frac{\partial B_y}{\partial R} \right|_{R_0} \\
 B_R(0 + y) &= y \underbrace{\left. \frac{\partial B_R}{\partial y} \right|_0}_{= \left. \frac{\partial B_y}{\partial R} \right|_{R_0}} + \frac{y^3}{3!} \left. \frac{\partial^3 B_R}{\partial y^3} \right|_0 + \dots \approx y \left. \frac{\partial B_y}{\partial R} \right|_{R_0}
 \end{aligned} \quad (3.7)$$

1673 Using these, and noting $(\dot{*}) = d(*)/dt$, the linear approximation of the differential
 1674 equations of motion in the moving frame writes

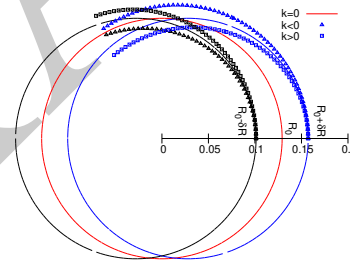
$$\begin{aligned}
 F_x = m\ddot{x} &= -qvB_y(R) + \frac{mv^2}{R_0 + x} \approx -qv \left(B_y(R_0) + \left. \frac{\partial B_y}{\partial R} \right|_{R_0} x \right) + \frac{mv^2}{R_0} \left(1 - \frac{x}{R_0} \right) \\
 \rightarrow m\ddot{x} &= -\frac{mv^2}{R_0^2} \left(\frac{R_0}{B_0} \left. \frac{\partial B_y}{\partial R} \right|_{R_0} + 1 \right) x \quad (3.8) \\
 F_y = m\ddot{y} &= qvB_R(y) = qv \left. \frac{\partial B_R}{\partial y} \right|_{y=0} y + \text{higher order} \rightarrow m\ddot{y} = qv \frac{\partial B_y}{\partial R} y
 \end{aligned}$$

Fig. 3.9 Axial motion stability requires proper shaping of field lines: B_y has to decrease with radius. The Laplace force pulls a positive charge with velocity pointing out of the page, at I, toward the median plane. Increasing the field gradient (k closer to -1 , gap opening up faster) increases the focusing



1675

Fig. 3.10 Geometrical focusing: take $k=0$; two circular trajectories which start from $r = R_0 \pm \delta R$ (solid lines, going counter-clockwise) undergo exactly one oscillation around the reference orbit $r = R_0$. A negative k (triangles), for axial focusing, decreases the radial convergence; a positive k (square markers) increases the radial convergence - and increases vertical divergence



1676

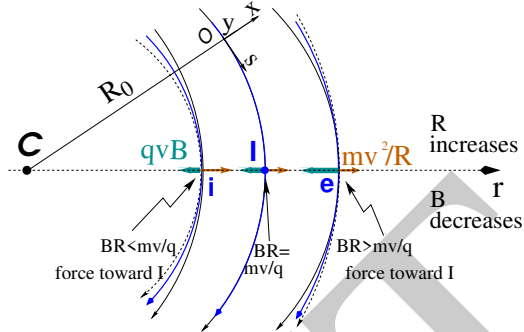
Note $B_y(R_0) = B_0$ and introduce

$$\omega_R^2 = \omega_{\text{rev}}^2 \left(1 + \frac{R_0}{B_0} \frac{\partial B_y}{\partial R} \right), \quad \omega_y^2 = -\omega_{\text{rev}}^2 \frac{R_0}{B_0} \frac{\partial B_y}{\partial R} \quad (3.9)$$

1677

substitute in Eqs. 3.8, this yields

Fig. 3.11 Radial motion stability. Trajectory arcs at $p = mv$ are represented: case of $k = 0$ (thin black lines), of $-1 < k < 0$ (thick blue lines), and of $k = -1$ (dashed concentric circles). k decreasing towards -1 reduces the geometrical focusing, increases axial focusing. The resultant of the Laplace and centrifugal forces, $F_t = -qvB + mv^2/r$, is zero at I, motion is stable if F_t is toward I at i , i.e. $qvB_i < mv^2/R_i$, and toward I as well at e , i.e. $qvB_e > mv^2/R_e$



$$\ddot{x} + \omega_R^2 x = 0 \quad \text{and} \quad \ddot{y} + \omega_y^2 y = 0 \quad (3.10)$$

1678 A restoring force (linear terms in x and y , Eq. 3.10) arises from the radially varying
1679 field, characterized by a field index

$$k = \frac{R_0}{B_0} \left. \frac{\partial B_y}{\partial R} \right|_{R=R_0, y=0} \quad (3.11)$$

1680 *Radial stability*: radially this force adds to the geometrical focusing (curvature term
1681 “1” in ω_R^2 , Eq. 3.9, Fig. 3.10). In the weakly decreasing field $B(R)$ an ion with mo-
1682 mentum $p = mv$ moving in the vicinity of the R_0 -radius reference orbit experiences
1683 in the moving frame a resultant force $F_t = -qvB + m \frac{v^2}{r}$ (Fig. 3.11) of which the
1684 (outward) component $f_c = m \frac{v^2}{r}$ decreases with r at a higher rate than the decrease
1685 of the Laplace (inward) component $f_B = -qvB(r)$. In other words, radial stability
1686 requires BR to increase with R , $\frac{\partial BR}{\partial R} = B + R \frac{\partial B}{\partial R} > 0$, this holds in particular at R_0 ,
1687 thus $1 + k > 0$.

1688 *Axial stability* requires a restoring force directed toward the median plane. Refer-
1689 ring to Fig. 3.9, this means $F_y = -a \times y$ (with a a positive quantity) and thus $B_R < 0$,
1690 at all $(r, y \neq 0)$. This is achieved by designing a guiding field which decreases with
1691 radius, $\frac{\partial B_R}{\partial y} < 0$. Referring to Eq. 3.11 this means $k < 0$.

1692 From these radial and axial constraints the condition of “weak focusing” for
1693 transverse motion stability around the circular equilibrium orbit results, namely,

$$-1 < k < 0 \quad (3.12)$$

1694 Note regarding the geometrical focusing: the focal distance associated with the
1695 curvature of a magnet of arc length \mathcal{L} is obtained by integrating $\frac{d^2 x}{ds^2} + \frac{1}{R_0^2} x = 0$ and
1696 identifying with the focusing property $\Delta x' = -x/f$, namely,

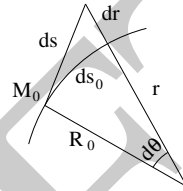
$$\Delta x' = \int \frac{d^2 x}{ds^2} ds \approx \frac{-x}{R^2} \int ds = \frac{-x \mathcal{L}}{R^2}, \text{ thus } f = \frac{R^2}{\mathcal{L}} \quad (3.13)$$

1697 *Isochronism*: the axial focusing constraint, B decreasing with R , contributes break-
 1698 ing the isochronism (in addition to the effect of the mass increase) by virtue of
 1699 $\omega_{\text{rev}} \propto B$.

1700 Paraxial Transverse Coordinates

1701 Introduce the path variable s as the independent variable in Eq. 3.10 and neglect the
 1702 transverse velocity components ($1 + \frac{x}{R_0} \approx 1$, $y \ll 0$) so that

$$ds = [r^2(s)d\theta^2 + dr^2 + dy^2]^{1/2} \approx |\mathbf{v}|dt \quad (3.14)$$



1703 thus the equations of motion in the moving frame (Eq. 3.10) take the form

$$\frac{d^2 x}{ds^2} + \frac{1+k}{R_0^2} x = 0 \quad \text{and} \quad \frac{d^2 y}{ds^2} - \frac{k}{R_0^2} y = 0 \quad (3.15)$$

1704 Given $-1 < k < 0$ the motion is that of a harmonic oscillator, in both planes, with
 1705 respective restoring constants $(1+k)/R_0^2$ and $-k/R_0^2$, both positive quantities. The
 1706 solution is a sinusoidal motion,

$$\begin{cases} r(s) - R_0 = x(s) = x_0 \cos \frac{\sqrt{1+k}}{R_0}(s - s_0) + x'_0 \frac{R_0}{\sqrt{1+k}} \sin \frac{\sqrt{1+k}}{R_0}(s - s_0) \\ r'(s) = x'(s) = -x_0 \frac{\sqrt{1+k}}{R_0} \sin \frac{\sqrt{1+k}}{R_0}(s - s_0) + x'_0 \cos \frac{\sqrt{1+k}}{R_0}(s - s_0) \end{cases} \quad (3.16)$$

$$\begin{cases} y(s) = y_0 \cos \frac{\sqrt{-k}}{R_0}(s - s_0) + y'_0 \frac{R_0}{\sqrt{-k}} \sin \frac{\sqrt{-k}}{R_0}(s - s_0) \\ y'(s) = -y_0 \frac{\sqrt{-k}}{R_0} \sin \frac{\sqrt{-k}}{R_0}(s - s_0) + y'_0 \cos \frac{\sqrt{-k}}{R_0}(s - s_0) \end{cases} \quad (3.17)$$

1708 Radial and axial wave numbers can be introduced,

$$\nu_R = \frac{\omega_R}{\omega_{\text{rev}}} = \sqrt{1+k} \quad \text{and} \quad \nu_y = \frac{\omega_y}{\omega_{\text{rev}}} = \sqrt{-k} \quad (3.18)$$

1709 *i.e.*, the number of sinusoidal oscillations of the paraxial motion about the reference
 1710 circular orbit over a turn, respectively radial and axial. Both are less than 1: there
 1711 is less than one sinusoidal oscillation in a revolution. In addition, as a result of the
 1712 revolution symmetry of the field,

$$\nu_R^2 + \nu_y^2 = 1 \quad (3.19)$$

1713 *Off-Momentum Orbit*

In a structure with revolution symmetry, the equilibrium trajectory at momentum

$$\begin{cases} p_0 \\ p = p_0 + \Delta p \end{cases} \text{ is at radius } \begin{cases} R_0 \text{ with } B_0 R_0 = \frac{p_0}{q} \\ R \text{ with } BR = \frac{p}{q} \end{cases}, \text{ where } \begin{cases} B = B_0 + \left(\frac{\partial B}{\partial x}\right)_0 \Delta x + \dots \\ R = R_0 + \Delta x \end{cases}$$

On the other hand

$$BR = \frac{p}{q} \Rightarrow \left[B_0 + \left(\frac{\partial B}{\partial x}\right)_0 \Delta x + \dots \right] (R_0 + \Delta x) = \frac{p_0 + \Delta p}{q}$$

1714 which, neglecting terms in $(\Delta x)^2$, and given $B_0 R_0 = \frac{p_0}{q}$, leaves $\Delta x \left[\left(\frac{\partial B}{\partial x}\right)_0 R_0 + B_0 \right] = \frac{\Delta p}{q}$. With $k = \frac{R_0}{B_0} \left(\frac{\partial B}{\partial x}\right)_0$ this yields

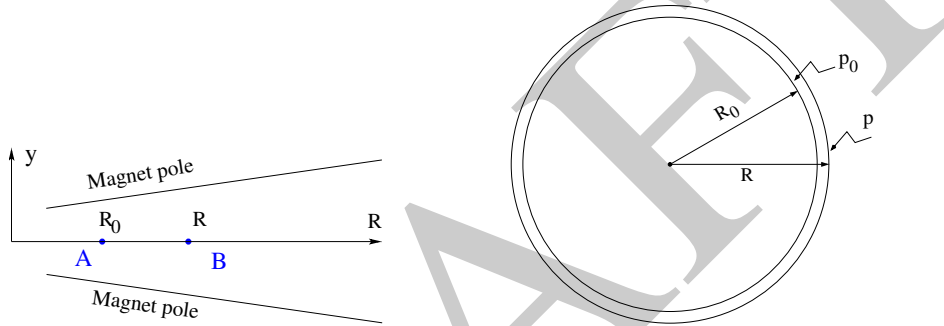


Fig. 3.12 The equilibrium radius at location A is R_0 , momentum is p_0 , rigidity is $B_0 R_0$. The equilibrium radius at B is R , momentum p , rigidity BR

1715

$$\Delta x = D \frac{\Delta p}{p_0} \quad \text{with} \quad D = \frac{R_0}{1+k} \quad \text{the dispersion function} \quad (3.20)$$

1716 The dispersion D is an s -independent quantity as a result of the revolution symmetry
1717 of the field (k and $R=p/qB$ are s -independent).

1718 To the first order in the coordinates, the vertical coordinates $y(s)$, $y'(s)$ (Eq. 3.17)
1719 are unchanged under the effect of a momentum offset, the horizontal trajectory angle
1720 $x'(s)$ (Eq. 3.16) is unchanged as well (the circular orbits are concentric, Fig. 3.12)
1721 whereas $x(s)$ satisfies

$$x(s, p_0 + \Delta p) = x(s, p_0) + \Delta p \left. \frac{\partial x}{\partial p} \right|_{s, p_0} = x(s, p_0) + D \frac{\Delta p}{p_0} \quad (3.21)$$

1722 *Orbit and revolution period lengthening*

1723 A δp momentum offset results in (Eq. 3.20)

$$\frac{\delta C}{C} = \frac{\delta R}{R} = \frac{\delta x}{R} = \alpha \frac{\delta p}{p} \quad \text{with} \quad \alpha = \frac{1}{1+k} = \frac{1}{\gamma^2 R} \quad (3.22)$$

1724 with α the momentum compaction, a positive quantity: orbit length increases with
1725 momentum. Substituting $\frac{\delta \beta}{\beta} = \frac{1}{\gamma^2} \frac{\delta p}{p}$, the change in revolution period $T_{\text{rev}} = C/\beta c$
1726 with momentum writes

$$\frac{\delta T_{\text{rev}}}{T_{\text{rev}}} = \frac{\delta C}{C} - \frac{\delta \beta}{\beta} = \left(\alpha - \frac{1}{\gamma^2} \right) \frac{\delta p}{p} \quad (3.23)$$

1727 Given that $-1 < k < 0$ and $\gamma \gtrsim 1$, it results that $\alpha - 1/\gamma^2 > 0$: the revolution period
1728 increases with energy, the increase in radius is faster than the velocity increase.

1729 3.2.3 Quasi-Isochronous Resonant Acceleration

1730 The energy W of an accelerated ion (in the non-relativistic energy domain of the
1731 classical cyclotron) satisfies the frequency dependence

$$W = \frac{1}{2} m v^2 = \frac{1}{2} m (2\pi R f_{\text{rev}})^2 = \frac{1}{2} m \left(2\pi R \frac{f_{\text{rf}}}{h} \right)^2 \quad (3.24)$$

1732 Observe in passing: given the cyclotron size (radius R), f_{rf} and h set the limit for
1733 the acceleration range. The revolution frequency decreases with energy and the
1734 condition of synchronism with the oscillating voltage, $f_{\text{rf}} = h f_{\text{rev}}$, is only fulfilled
1735 at that particular radius where $\omega_{\text{rf}} = qB/m$ (Fig. 3.13-left). The out-phasing $\Delta\phi$ of
1736 the RF at ion arrival at the gap builds-up turn after turn, decreasing in a first stage
1737 (towards lower voltages in Fig. 3.13-right) and then increasing back to $\phi = \pi/2$ and
1738 beyond towards π . Beyond $\phi = \pi$ the RF voltage is decelerating.

1739 With ω_{rev} constant between two gap passages, differentiating $\phi(t)$ (Eq. 3.2) yields
1740 $\dot{\phi} = \omega_{\text{rf}} - \omega_{\text{rev}}$. Between two gap passages on the other hand, $\Delta\phi = \dot{\phi}\Delta T = \dot{\phi}T_{\text{rev}}/2 =$
1741 $\dot{\phi} \frac{\pi R}{v}$, yielding a phase-shift of

$$\text{half-turn} \quad \Delta\phi = \pi \left(\frac{\omega_{\text{rf}}}{\omega_{\text{rev}}(R)} - 1 \right) = \pi \left(\frac{m\omega_{\text{rf}}}{qB(R)} - 1 \right) \quad (3.25)$$

1742 The out-phasing is thus a gap-after-gap, cumulative effect. Due to this the classical
1743 cyclotron requires quick acceleration (small number of turns), which means high
1744 voltage (tens to hundreds of kVolts). As expected, with ω_{rf} and B constant, ϕ presents
1745 a minimum ($\dot{\phi} = 0$) at $\omega_{\text{rf}} = \omega_{\text{rev}} = qB/m$ where exact isochronism is reached
1746 (Fig. 3.13). The upper limit to ϕ is set by the condition $\Delta W > 0$: acceleration.

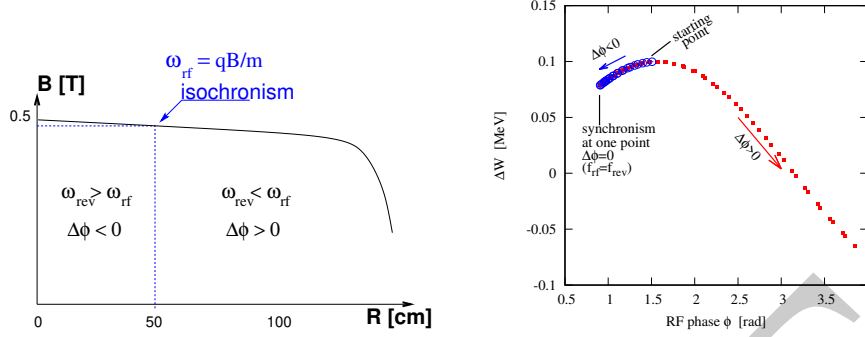
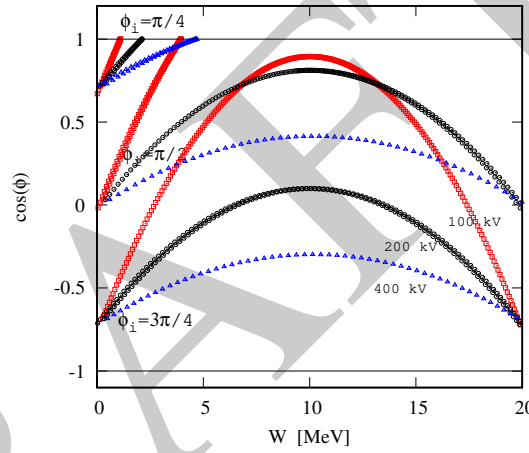


Fig. 3.13 Left: a sketch of the synchronism condition at one point ($h=1$ assumed). Right: the span in phase of the energy gain $\Delta W = q\hat{V} \sin \phi$ (Eq. 3.2) over the acceleration cycle

Fig. 3.14 A graph of the cyclotron equation (Eq. 3.26), for three different accelerating voltages: 100, 200 and 400 kV/gap (respectively square, circle and triangle markers). The sole settings resulting in $-1 < \cos \phi(E) < 1$, $\forall E$, allow complete acceleration to top energy. $\phi_i = \pi/4$ at injection for instance, does not (upper three curves). $\phi_i = 3\pi/4$ works (lower three curves), with as low as 100 kV/gap



1747 The cyclotron equation determines the achievable energy range, depending on
 1748 the injection energy E_i , the RF phase at injection ϕ_i , the RF frequency ω_{rf} and gap
 1749 voltage \hat{V} . It writes [12]

$$\cos \phi = \cos \phi_i + \pi \left[1 - \frac{\omega_{rf}}{\omega_{rev}} \frac{E + E_i}{2M} \right] \frac{E - E_i}{q\hat{V}} \quad (3.26)$$

1750 Equation 3.26 is represented in Fig. 3.14 for various values of the peak voltage
 1751 and phase at injection ϕ_i . M [eV/c²] and E [eV] are respectively the rest mass and
 1752 relativistic energy, $q\hat{V}$ is expressed in electron-volts, the index i denotes injection
 1753 parameters.

1754 3.2.4 Beam Extraction

1755 From $R = p/qB$ and assuming $B(R) \approx \text{constant}$ (this is legitimate as k is normally
1756 small), in the non-relativistic approximation ($W \ll M$, $W = p^2/2M$) one gets

$$\frac{dR}{R} = \frac{1}{2} \frac{dW}{W} \quad (3.27)$$

1757 Integrating yields

$$R^2 = R_i^2 \frac{W}{W_i} \quad (3.28)$$

1758 with R_i, W_i initial conditions. From Eqs. 3.27, 3.28, assuming $W_i \ll W$ and constant
1759 acceleration rate dW such that $W = n dW$ after n turns, one gets the scaling laws

$$R \propto \sqrt{n}, \quad dR \propto \frac{R}{W} \propto \frac{1}{R} \propto dW, \quad \frac{dR}{dn} = \frac{R}{2n} \quad (3.29)$$

1760 The turn separation dR is proportional to the energy gain per turn and inversely
1761 proportional to the orbit radius.

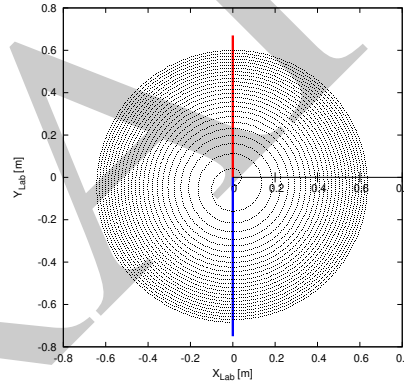


Fig. 3.15 The radial distance between successive turns decreases with energy, in inverse proportion to the orbit radius. The red and blue segments here figure the accelerating gap

1762 The radial distance between successive turns decreases with energy, toward zero
1763 (Fig. 3.15), eventually resulting in insufficient spacing for insertion of an extraction
1764 septum.

1765 *Orbit modulation*

1766 Consider an ion bunch injected in the cyclotron with some (x_0, x'_0) conditions in
1767 the vicinity of the reference orbit, and assume slow acceleration. While accelerated
1768 the bunch undergoes an oscillatory motion around the equilibrium orbit (Eq. 3.16).
1769 Observed at the extraction septum this oscillation modulates the distance of the

1770 bunch to the local equilibrium orbit, moving it outwards or inwards depending on
 1771 the turn number, which modulates the distance between the accelerated turns. This
 1772 effect can be resorted to, so to increase the separation between the final two turns
 1773 and so enhance the extraction efficiency [9].

1774 3.2.5 Spin Dance

1775 “Much of the physics of spin motion can be illustrated using the simplest model of a
 1776 storage ring consisting of uniform horizontal bending and no straight sections.” [13].

1777 By virtue of this statement, a preliminary introduction to spin motion in magnetic
 1778 fields is given in the present chapter. In support to this in addition, comes the fact that
 1779 cyclotrons happened to be the first circular machines to accelerate polarized beams
 1780 (first acceleration of polarized beams had happened earlier in the 1960s, using
 1781 electrostatic columns at voltage generators, when polarized proton and deuteron
 1782 sources began operating [14]).

1783 The magnetic field \mathbf{B} of the cyclotron dipole exerts a torque on the spin angular
 1784 momentum \mathbf{S} of an ion, causing it to precess following the Thomas-BMT differential
 1785 equation [15]

$$\frac{d\mathbf{S}}{dt} = \mathbf{S} \times \underbrace{\frac{q}{m} [(1+G)\mathbf{B}_{\parallel} + (1+G\gamma)\mathbf{B}_{\perp}]}_{\omega_{\text{sp}}} \quad (3.30)$$

1786 where t is the time; ω_{sp} the precession vector: a combination of \mathbf{B}_{\parallel} and \mathbf{B}_{\perp} compo-
 1787 nents of \mathbf{B} respectively parallel and orthogonal to the ion velocity vector. G is the
 1788 gyromagnetic anomaly,

1789 $G=1.7928474$ (proton), -0.178 (Li), -0.143 (deuteron), -4.184 (^3He) ...

1790 \mathbf{S} in this equation is in the ion rest frame, all other quantities are in the laboratory
 1791 frame.

1792 In the case of an ion moving in the median plane of the dipole, $\mathbf{B}_{\parallel} = 0$, thus the
 1793 precession axis is parallel to the magnetic field vector, \mathbf{B}_y , so that $\omega_{\text{sp}} = \frac{q}{m} (1 +$
 1794 $G\gamma)\mathbf{B}_y$. The spin precession angle over a trajectory arc \mathcal{L} is

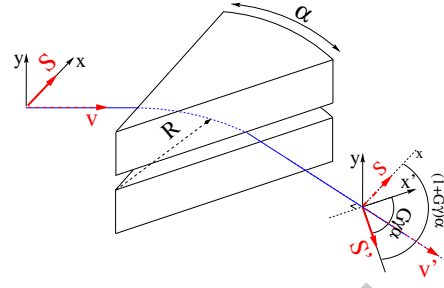
$$\theta_{\text{sp, Lab}} = \frac{1}{v} \int_{(\mathcal{L})} \omega_{\text{sp}} ds = (1+G\gamma) \frac{\int_{(\mathcal{L})} B ds}{BR} = (1+G\gamma)\alpha \quad (3.31)$$

1795 with α the velocity vector precession (Fig. 3.16). The precession angle in the moving
 1796 frame (the latter rotates by an angle α along \mathcal{L}) is

$$\theta_{\text{sp}} = G\gamma\alpha \quad (3.32)$$

1797 thus the number of 2π spin precessions per ion orbit around the cyclotron is $G\gamma$. By
 1798 analogy with the wave numbers (Eq. 3.18) this defines the “spin tune”

Fig. 3.16 Spin and velocity vector precession in a constant field, from \mathbf{S} to \mathbf{S}' and \mathbf{v} to \mathbf{v}' respectively. In the moving frame the spin precession along the arc $\mathcal{L} = R\alpha$ is $G\gamma\alpha$, in the laboratory frame the spin precesses by $(1 + G\gamma)\alpha$



$$v_{\text{sp}} = G\gamma$$

(3.33)

DRAFT

1799 3.3 Exercises

1800 Note: some of the input data files for these simulations are available in zgoubi
1801 sourceforge repository at

https://sourceforge.net/p/zgoubi/code/HEAD/tree/branches/exemples/book/zgoubiMaterial/cyclotron_classical/

1803 3.1 Modeling a Cyclotron Dipole: Using a Field Map

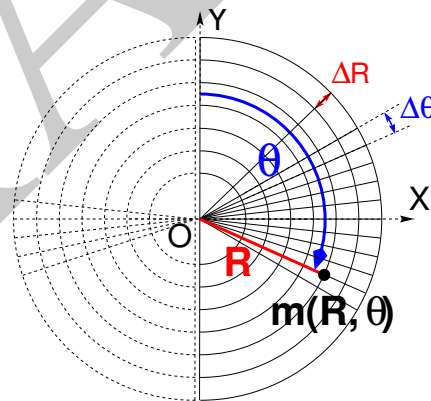
1804 Solution: page 71

1805 In this exercise, ion trajectories are ray-traced, various optical properties addressed in
1806 the foregoing are recovered, using a field map to simulate the cyclotron dipole.
1807 Fabricating that field map is a preliminary step of the exercise.

1808 The interest of using a field map is that it is an easy way to account for fancy
1809 magnet geometries and fields, including field gradients and possible defects. A
1810 field map can be generated using mathematical field models, or from magnet com-
1811 putation codes, or from magnetic measurements. The first method is used, here.
1812 TOSCA[MOD.MOD1=22.1] keyword [16, cf. INDEX] is used to ray-trace through
1813 the map.

1814 *Working hypotheses:* A 2-dimensional $m(R, \theta)$ polar meshing of the median plane
1815 is considered (Fig. 3.17). It is defined in a $(O; X, Y)$ frame and covers an angular
1816 sector of a few tens of degrees. The mid-plane field map is the set of values $B_z(R, \theta)$
1817 at the nodes of the mesh. During ray-tracing, TOSCA[MOD.MOD1=22.1] extrapolates
1818 the field along 3D space (R, θ, Z) ion trajectories from the 2D polar map [16].

Fig. 3.17 Principle of a 2D field map in polar coordinates, covering a 180° sector (over the right hand side dee). The mesh nodes $m(R, \theta)$ are distant ΔR radially, $\Delta\theta$ azimuthally. The map is used twice to cover the 360° cyclotron dipole as sketched here, while allowing insertion of an accelerating gap between the two dees



1819 (a) Construct a 180° two-dimensional map of a median plane field $B_z(R, \theta)$,
1820 proper to simulate the field in a cyclotron as sketched in Fig. 3.1. Use one of
1821 the following two methods: either (i) write an independent program, or (ii) use
1822 zgoubi and its analytical field model DIPOLE, together with the keyword OP-
1823 TIONS[CONSTY=ON] [16, cf. INDEX].

1824 Besides: use a uniform mesh (Fig. 3.17) covering from $R_{\min}=1$ to $R_{\max}=76$ cm,
1825 with radial increment $\Delta R = 0.5$ cm, azimuthal increment $\Delta\theta = 0.5$ [cm]/ R_0 with R_0

1826 some reference radius (say, 50 cm, in view of subsequent exercises), and constant
 1827 axial field $B_Z = 5$ kG. The appropriate 6-column formatting of the field map data
 1828 for TOSCA[MOD.MOD1=22.1] to read is the following:

1829 $R \cos \theta, Z, R \sin \theta, BY, BZ, BX$

1830 with θ varying first, R varying second; Z is the vertical direction (normal to the map
 1831 mesh), $Z \equiv 0$ in the present case. Note that proper functioning of TOSCA requires
 1832 the field map to begin with the following line of numerical values:

1833 Rmin [cm] ΔR [cm] $\Delta \theta$ [deg] Z [cm]

1834 Produce a graph of the $B_Z(R, \theta)$ field map content.

1835 (b) Ray-trace a few concentric circular mid-plane trajectories centered on the
 1836 center of the dipole, ranging in $10 \leq R \leq 80$ cm. Produce a graph of these concentric
 1837 trajectories in the $(O; X, Y)$ laboratory frame.

1838 Initial coordinates can be defined using OBJET, particle coordinates along tra-
 1839 jectories during the stepwise ray-tracing can be logged in zgoubi.plt by setting IL=2
 1840 under TOSCA. In order to find the Larmor radius corresponding to a particular
 1841 momentum, the matching procedure FIT can be used. In order to repeat the latter for
 1842 a series of different momenta, REBELOTE[IOPT=1] can be used.

1843 Explain why it is possible to push the ray-tracing beyond the 76 cm radial extent
 1844 of the field map.

1845 (c) Compute the orbit radius R and the revolution period T_{rev} as a function of
 1846 kinetic energy W or rigidity BR . Produce a graph, including for comparison the
 1847 theoretical dependence of T_{rev} .

1848 (d) Check the effect of the density of the mesh (the choice of ΔR and $\Delta \theta$ values,
 1849 *i.e.*, the number of nodes $N_\theta \times N_R = (1 + \frac{180^\circ}{\Delta \theta}) \times (1 + \frac{80 \text{ cm}}{\Delta R})$), on the accuracy of the
 1850 trajectory and time-of-flight computation.

1851 (e) Check the effect of the integration step size on the accuracy of the trajectory
 1852 and time-of-flight computation, by considering a small $\Delta s = 1$ cm and a large
 1853 $\Delta s = 10$ cm, at 200 keV and 5 MeV (proton), and comparing with theory.

1854 (f) Consider a periodic orbit, thus its radius R should remain unchanged after
 1855 stepwise integration of the motion over a turn. However, the size Δs of the numerical
 1856 integration step has an effect on the final value of the radius:

1857 For two different cases, 200 keV (a small orbit) and 5 MeV (a larger one), provide a
 1858 graph of the dependence of the relative error $\delta R/R$ after one turn, on the integration
 1859 step size Δs (consider a series of Δs values in a range $\Delta s : 0.1 \text{ mm} \rightarrow 20 \text{ cm}$).
 1860 REBELOTE[IOPT=1] do-loop can be used to repeat the one-turn raytracing with
 1861 different Δs .

1862 3.2 Modeling a Cyclotron Dipole: Using an Analytical Field Model

1863 Solution: page 80

1864 This exercise is similar to exercise 3.1, yet using the analytical modeling DIPOLE,
 1865 instead of a field map. DIPOLE provides the Z -parallel median plane field $\mathbf{B}(R, \theta, Z =$
 1866 $0) \equiv \mathbf{B}_Z(R, \theta, Z = 0)$ at the projected $m(R, \theta, Z = 0)$ ion location (Fig. 3.18), while
 1867 $\mathbf{B}(R, \theta, Z)$ at particle location is obtained by extrapolation.

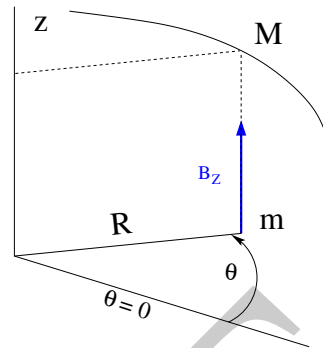


Fig. 3.18 DIPOLE provides the value $B_Z(m)$ of the median plane field at m , projection of particle position $M(R, \theta, Z)$ in the median plane. $\mathbf{B}(R, \theta, Z)$ is obtained by extrapolation

1868 (a) Simulate a 180° sector dipole; DIPOLE requires a reference radius [16,
1869 Eqs. 6.3.19-21], noted R_0 here; for the sake of consistency with other exercises, it is
1870 suggested to take $R_0 = 50$ cm. Take a constant axial field $B_Z = 5$ kG.

1871 Explain the various data that define the field simulation in DIPOLE: geometry,
1872 role of R_0 , field and field indices, fringe fields, integration step size, etc.

1873 Produce a graph of $B_Z(R, \theta)$.

1874 (b) Repeat question (b) of exercise 3.1.

1875 (c) Repeat question (c) of exercise 3.1.

1876 (d) As in question (e) of exercise 3.1, check the effect of the integration step size
1877 on the accuracy of the trajectory and time-of-flight computation.

1878 Repeat question (f) of exercise 3.1.

1879 (e) From the two series of results (exercise 3.1 and the present one), comment on
1880 various pros and cons of the two methods, field map versus analytical field model.

1881 3.3 Resonant Acceleration

1882 Solution: page 84

1883 Based on the earlier exercises, using indifferently a field map (TOSCA) or an
1884 analytical model of the field (DIPOLE), introduce a sinusoidal voltage between the
1885 two dees, with peak value 100 kV. Assume that ion motion does not depend on RF
1886 phase: the boost through the gap is the same at all passes, use CAVITE[IOPT=3] [16,
1887 cf. INDEX] for that. Note that using CAVITE requires prior PARTICUL in order to
1888 specify ion species and data, necessary to compute the energy boost (Eq. 3.2).

1889 (a) Accelerate a proton with initial kinetic energy 20 keV, up to 5 MeV, take
1890 harmonic $h=1$. Produce a graph of the accelerated trajectory in the laboratory frame.

1891 (b) Provide a graph of the proton momentum p and total energy E as a function
1892 of its kinetic energy, both from this numerical experiment (ray-tracing data can be
1893 stored using FAISTORE) and from theory, all on the same graph.

1894 (c) Provide a graph of the normalized velocity $\beta = v/c$ as a function of kinetic
1895 energy, both numerical and theoretical, and in the latter case both classical and
1896 relativistic.

1897 (d) Provide a graph of the relative change in velocity $\Delta\beta/\beta$ and orbit length $\Delta C/C$
 1898 as a function of kinetic energy, both numerical and theoretical. From their evolution,
 1899 conclude that the time of flight increases with energy.

1900 (e) Repeat the previous questions, assuming a harmonic $h=3$ RF frequency.

1901 3.4 Spin Dance

1902 Solution: page 88

1903 Cyclotron modeling in the present exercise can use Exercise 3.1 or Exercise 3.2
 1904 technique (*i.e.*, a field map or an analytical field model), indifferently.

1905 (a) Add spin transport, using SPNTRK [16, *cf.* INDEX]. Produce a listing
 1906 (zgoubi.res) of a simulation, including spin outcomes.

1907 Note: PARTICUL is necessary here, for the spin equation of motion (Eq. 3.30) to
 1908 be solved [16, Sect. 2]. SPNPRT can be used to have local spin coordinates listed in
 1909 zgoubi.res (at the manner that FAISCEAU lists local particle coordinates).

1910 (b) Consider proton case, take initial spin longitudinal, compute the spin preces-
 1911 sion over one revolution, as a function of energy over a range 12 keV \rightarrow 5 MeV. Give
 1912 a graphical comparison with theory.

1913 FAISTORE can be used to store local particle data, which include spin coord-
 1914 inates, in a zgoubi.fai style output file. IL=2 [16, *cf.* INDEX] (under DIPOLE or
 1915 TOSCA, whichever modeling is used) can be used to obtain a print out of particle
 1916 and spin motion data to zgoubi.plt during stepwise integration.

1917 (c) Inject a proton with longitudinal initial spin S_i . Give a graphic of the lon-
 1918 gitudinal spin component value as a function of azimuthal angle, over a few turns
 1919 around the ring. Deduce the spin tune from this computation. Repeat for a couple of
 1920 different energies.

1921 Place both FAISCEAU and SPNPRT commands right after the first dipole sector,
 1922 and use them to check the spin rotation and its relationship to particle rotation, right
 1923 after the first passage through that first sector.

1924 (d) Spin dance: the input data file optical sequence here is assumed to model a
 1925 full turn. Inject an initial spin at an angle from the horizontal plane (this is in order
 1926 to have a non-zero vertical component), produce a 3-D animation of the spin dance
 1927 around the ring, over a few turns.

1928 (e) Repeat questions (b-d) for two additional ions: deuteron (much slower spin
 1929 precession), ${}^3\text{He}^{2+}$ (much faster spin precession).

1930 3.5 Synchronized Spin Torque

1931 Solution: page 94

1932 A synchronized spin kick is superimposed on orbital motion. An input data file for
 1933 a complete cyclotron is considered as in question 3.4 (d), for instance six 60 degree
 1934 DIPOLES, or two 180 degree DIPOLES.

1935 Insert a local spin rotation of a few degrees around the longitudinal axis, at the
 1936 end of the optical sequence (*i.e.*, after one orbit around the cyclotron). SPINR can be
 1937 used for that, rather than a local magnetic field, so to avoid any orbital effect. Track
 1938 4 particles on their respective equilibrium orbit, with energies 0.2, 108.412, 118.878
 1939 and 160.746 MeV.

1940 Produce a graph of the motion of the vertical spin component S_y along the circular
1941 orbit.

1942 Produce a graph of the spin vector motion on a sphere.

1943 3.6 Weak Focusing

1944 Solution: page 97

1945 (a) Consider a 60° sector as in earlier exercises (building a field map and using
1946 TOSCA as in exercise 3.1, or using DIPOLE as in exercise 3.2), construct the sector
1947 accounting for a non-zero radial index k in order to introduce axial focusing, say
1948 $k = -0.03$, assume a reference radius R_0 for a reference energy of 200 keV (R_0 and
1949 B_0 are required in order to define the index k , Eq. 3.11). Ray-trace that 200 keV
1950 reference orbit, plot it in the lab frame: make sure it comes out as expected, namely,
1951 constant radius, final and initial angles zero.

1952 (b) Using FIT[2], find and plot the radius dependence of orbit rigidity, $BR(R)$,
1953 from ray-tracing over a BR range covering 20 keV to 5 MeV; superpose the theoretical
1954 curve. REBELOTE[IOPT=1] can be used to perform the scan.

1955 (c) Produce a graph of the paraxial axial motion of a 1 MeV proton, over a few
1956 turns (use IL=2 under TOSCA, or DIPOLE, to have step by step particle and field
1957 data logged in zgoubi.plt). Check the effect of the focusing strength by comparing
1958 the trajectories for a few different index values, including close to -1 and close to 0.

1959 (d) Produce a graph of the magnetic field experienced by the ion along these
1960 trajectories.

1961 3.7 Loss of Isochronism

1962 Solution: page 106

1963 Compare on a common graphic the revolution period $T_{\text{rev}}(R)$ for a field index
1964 value $k \approx -0.95, -0.5, -0.03, 0^-$. The scan method of exercise 3.6, based on
1965 REBELOTE[IOPT=1] preceded by FIT[2], can be referred to.

1966 3.8 Ion Trajectories

1967 Solution: page 108

1968 In this exercise individual ion trajectories are computed. DIPOLE or TOSCA
1969 magnetic field modeling can be used, indifferently. No acceleration here, ions circle
1970 around the cyclotron at constant energy.

1971 (a) Produce a graph of the horizontal $x(s)$ and vertical $y(s)$ trajectory coordinates
1972 of an ion with rigidity close to $BR(R_0)$ (R_0 is the reference radius in the definition of
1973 the index k), over a few turns around the cyclotron. From the number of turns, give
1974 an estimate of the wave numbers. Check the agreement with the expected $\nu_R(k)$,
1975 $\nu_y(k)$ values (Eq. 3.18).

1976 (b) Consider now protons at 1 MeV and 5 MeV, far from the reference energy
1977 $E(R_0)$; the wave numbers change with energy: consistency with theory can be
1978 checked. Find their theoretical values, compare with numerical outcomes.

1979 (c) Consider proton, 200 keV energy, plot as a function of s the difference between
1980 $x(s)$ from raytracing and its values from Eq. 3.16. Same for $y(s)$ compared to Eq. 3.17.

1981 IL=2 can be used to store in zgoubi.plt the step-by-step particle coordinates across
1982 DIPOLE.

1983 (d) Perform a scan of the wave numbers over 200 keV–5 MeV energy inter-
1984 val, computed using OBJET[KOBJ=5] and MATRIX[IORD=1,IFOC=11], or OB-
1985 JET[KOBJ=6] and MATRIX[IORD=2,IFOC=11], together with REBELOTE[IOPT=1]
1986 to repeat MATRIX for a series of energy values.

1987 3.9 RF Phase at the Accelerating Gap

1988 Solution: page 114

1989 Consider the cyclotron model of exercise 3.6: field index $k = -0.03$ defined at
1990 $R_0 = 50$ cm, field $B_0 = 5$ kG on that radius. two dees, double accelerating gap.

1991 Accelerate a proton from 1 to 5 MeV: get the turn-by-turn phase-shift at the gaps;
1992 use CAVITE[IOPT=7] to simulate the acceleration. Compare the half-turn $\Delta\phi$ so
1993 obtained with the theoretical expectation (Eq. 3.25). Produce similar graphs $B(R)$
1994 and $\Delta W(\phi)$ to Fig. 3.13.

1995 Accelerate over more turns, observe the particle decelerating.

1996 3.10 The Cyclotron Equation

1997 Solution: page 116

1998 The cyclotron model of exercise 3.3 is considered: two dees, double accelerating
1999 gap, uniform field $B = 5$ kG, no field gradient needed here (no vertical motion).

2000 (a) Set up an input data file for the simulation of a proton acceleration from
2001 0.2 to 20 MeV. In particular, assume that $\cos(\phi)$ reaches its maximum value at
2002 $W_m = 10$ MeV; find the RF voltage frequency from $d(\cos \phi)/dW = 0$ at W_m .

2003 (b) Give a graph of the energy-phase relationship (Eq. 3.26), for $\phi_i = \frac{3\pi}{4}, \frac{\pi}{2}, \frac{\pi}{4}$,
2004 from both simulation and theory.

2005 3.11 Cyclotron Extraction

2006 Solution: page 118

2007 (a) Acceleration of a proton in a uniform field $B = 5$ kG is first considered (field
2008 hypotheses as in exercise 3.3). RF phase is ignored: CAVITE[IOPT=3] can be used
2009 for acceleration. Take a 100 kV gap voltage.

2010 Compute the distance ΔR between turns, as a function of turn number and of
2011 energy, over the range $E : 0.02 \rightarrow 5$ MeV. Compare graphically with theoretical
2012 expectation.

2013 (b) Assume a beam with Gaussian momentum distribution and *rms* momentum
2014 spread $\delta p/p = 10^{-3}$. An extraction septum is placed half-way between two successive
2015 turns, provide a graph of the percentage of beam loss at extraction, as a function of
2016 extraction turn number. COLLIMA can be used for that simulation and for particle
2017 counts, it also allows for possible septum thickness.

2018 (c) Repeat (a) and (b) considering a field with index: take for instance $B_0 = 5$ kG
2019 and $k = -0.03$ at $R_0 = R(0.2 \text{ MeV}) = 12.924888$ cm.

2020 (d) Investigate the effect of injection conditions (Y_i, T_i) on the modulation of the
2021 distance between turns.

2022 Try and confirm numerically that, with slow acceleration, the oscillation is mini-
2023 mized for an initial $|T_i| = \left| \frac{x_0 v_R}{R} \right|$ (after Ref. [9, p. 133]).

2024 3.12 Acceleration and Extraction of a 6-D Polarized Bunch

2025 Solution: page 123

2026 The cyclotron simulation hypotheses of exercise 3.10-a are considered; account
2027 or $k = -0.02$ field index.

2028 Add a short “high energy” extraction line, say 1 meter, following REBELOTE in
2029 the optical sequence, ending up with a “Beam_Dump” MARKER for instance.

2030 (a) Create a 1,000 ion bunch with the following initial parameters:

2031 - random Gaussian transverse phase space densities, centered on the equilibrium
2032 orbit, truncated at 3 sigma, normalized *rms* emittances $\varepsilon_Y = \varepsilon_Z = 1 \pi \mu\text{m}$, both
2033 emittances matched to the 0.2 MeV orbit optics,

2034 - uniform bunch momentum density $0.2 \times (1 - 10^{-3}) \leq p \leq 0.2 \times (1 + 10^{-3})$ MeV,
2035 matched to the dispersion, namely (Eq. 3.21), $\Delta x = D \frac{\Delta p}{p}$,

2036 - random uniform longitudinal distribution $-0.5 \leq s \leq 0.5$ mm,

2037 Note: two ways to create this object are, (i) using MCOBJET[KOBJ=3] which
2038 generates a random distribution, or (ii) using OBJET[KOBJ=3] to read an external
2039 particle coordinate file.

2040 Add spin tracking request (SPNTRK), all initial spins normal to the bend plane.

2041 Produce a graph of the three initial 2-D phase spaces: (Y,T), (Z,P), $(\delta l, \delta p/p)$,
2042 matched to the 200 keV periodic optics. Provide Y, Z, dp/p, δl and S_Z histograms
2043 (HISTO can be used), check the distribution parameters.

2044 (b) Accelerate this polarized bunch to 20 MeV, using the following RF conditions:

2045 - 200 kV peak voltage,

2046 - RF harmonic 1,

2047 - initial RF phase $\phi_i = \pi/4$.

2048 Produce a graph of the three phase spaces as observed downstream of the extrac-
2049 tion line. Provide the Y, Z, dp/p, δl and S_Z histograms. Compare the distribution
2050 parameters with the initial values.

2051 What causes the spins to spread away from vertical?

2052 3.4 Solutions of Exercises of Chapter 3: Classical Cyclotron

2053 3.1 Modeling a Cyclotron Dipole: Using a Field Map

2054

2055 (a) A field map of a 180° sector of a classical cyclotron magnet.

2056 The first option is retained here: a Fortran program, geneSectorMap.f, given in
2057 Tab. 3.1. constructs the required map of a field distribution $B_Z(R, \theta)$, to be subse-
2058 quently read and raytraced through using the keyword TOSCA [16, lookup INDEX].